Materials Science and Technology

ISSN: 0267-0836 (Print) 1743-2847 (Online) Journal homepage: http://www.tandfonline.com/loi/ymst20

Electron backscattering diffraction study of acicular ferrite, bainite, and martensite steel microstructures

Gourgues A.-F., H.M. Flower & T.C. Lindley

To cite this article: Gourgues A.-F., H.M. Flower & T.C. Lindley (2000) Electron backscattering diffraction study of acicular ferrite, bainite, and martensite steel microstructures, Materials Science and Technology, 16:1, 26-40, DOI: 10.1179/026708300773002636

To link to this article: http://dx.doi.org/10.1179/026708300773002636

Published online: 19 Jul 2013.

Submit your article to this journal

Article views: 1536

View related articles

Citing articles: 170 View citing articles

Full Terms & Conditions of access and use can be found at
http://www.tandfonline.com/action/journalInformation?journalCode=ymst20

Download by: [193.140.168.9] **Date:** 21 June 2017, At: 23:42

Electron backscattering diffraction study of acicular ferrite, bainite, and martensite steel microstructures

A.-F. Gourgues, H. M. Flower, and T. C. Lindley

This study deals with acicular ferrite, bainite, and martensite microstructures observed in three low alloy steels. Electron backscattering diffraction (EBSD) was used to assess crystallographic features of these microstructures. In each area studied by EBSD mapping, 'crystallographic packets' defined as clusters of points sharing the same crystallographic orientation were compared with 'morphological packets' observed in the corresponding light micrograph. Microtexture studies suggested that acicular ferrite and upper bainite grow with Nishiyama–Wassermann relationships with the parent austenite phase, whereas lower bainite and martensite consist of highly intricate packets having Kurdjumov–Sachs relationships with the parent phase. In all cases three highly misoriented texture components were found within each former austenite grain. Electron backscattering diffraction also gave information about the cleavage and intergranular reverse temper embrittlement fracture mechanisms of these steels. In conclusion, it is shown that EBSD is a powerful tool for studying phase transformation and fracture mechanisms in steels on a microscopic scale. **MST/4312**

Dr Gourgues is in the Ecole des Mines de Paris, Centre des Matériaux, UMR CNRS 7633, BP 87, 91003 Evry Cedex, France. Professor Flower and Professor Lindley are in the Department of Materials, Imperial College of Science, Technology and Medicine, Prince Consort Road, London SW7 2BP, UK. *Manuscript received 10 February 1999; accepted 19 April 1999.*
© 2000 IoM Communications Ltd.

Introduction

Electron backscattering diffraction (EBSD) has been found to be a powerful technique for studying the local crystallographic properties of a number of microstructures.[1,2] Most studies concerned with steels have been devoted to microtexture measurements and/or phase recognition[3,4] while others were concerned with deformation mechanisms[5,6] and strain measurements.[7] Studies related to the mechanisms of cleavage fracture in ferritic steels, and to the determination of the cleavage plane, have also been published.[8,9] However, very few EBSD results have been published on the microstructural features arising from the austenite to ferrite transformation (AFT) concerning Widmanstätten ferrite,[10] acicular ferrite,[11] or bainite.[9]

The aim of the present study is to show how the EBSD technique may give, with minimum specimen preparation, quantitative information about the microstructure produced by various AFT mechanisms in low alloy steels. In particular, a comparison will be made between different steel microstructures, namely, acicular ferrite, bainite, and martensite. Acicular ferrite is known to nucleate on intragranular inclusions; its high toughness is attributed to the chaotic arrangement of the ferrite plates. This microstructure is often encountered in weld metal deposits. Bainite and martensite are known to grow as packets of fine, nearly parallel laths and/or platelets, but differ in toughness and in sensitivity to reverse temper embrittlement (RTE).[12,13] The relationship between the grain (or packet) size and the mechanical properties of these microstructures is focused on in the present study. For this purpose, two types of grains (or packets) were defined. The 'crystallographic' grains and/or packets (referred to as 'crystallographic packets') correspond to grains, or sets of neighbouring units sharing the same crystallographic orientation. The 'morphological' grains and/or packets (referred to as 'morphological packets') were defined as sheaves of parallel units which may be observed in a light or scanning electron microscope after suitable metallographic preparation. In the present study, the crystallographic packet size was determined by EBSD, whereas the morphological packets were studied using light microscopy after nital etching. They were delimited by carbides, martensite–austenite (M–A) islands, and/or nital revealed boundaries. A comparison of both kinds of grains was then made for all microstructures examined.

In the present study, the EBSD technique was also used in order to assess the crystallographic features of brittle fracture in these microstructures. Two fracture mechanisms were considered, namely, cleavage fracture and intergranular (IG) fracture occurring after RTE. The present study focuses on the role played by the misorientation between adjacent crystallographic packets in the resistance of these steels to brittle fracture.

Materials and experimental procedures

MATERIALS

In order to separately study acicular ferrite, bainite, and martensite microstructures, three heats of low alloy steels were chosen. Their chemical compositions are given in Table 1, while the heat treatments are given in Table 2. Steel A is a low carbon steel containing titanium rich

Table 1 Chemical composition of steels used, wt-%

Steel	C	Si	Mn	P	S	Cr	Mo	Ni	Al	Co	Cu	Nb	Ti	V	B	Fe
A	0·072	0·250	1·610	0·016	0·005	0·046	0·008	0·033	0·010	0·007	0·069	0·002	0·014	0·008	0·0022	Bal.
B	0·070	0·320	1·500	0·012	0·001	0·059	0·119	0·468	0·027	…	0·164	0·014	0·002	0·002	0·0001	Bal.
C	0·200	0·250	1·380	0·017	0·009	0·150	0·490	0·830	0·024	…	0·140	0·006	0·005	0·005	…	Bal.

 ISSN 0267–0836

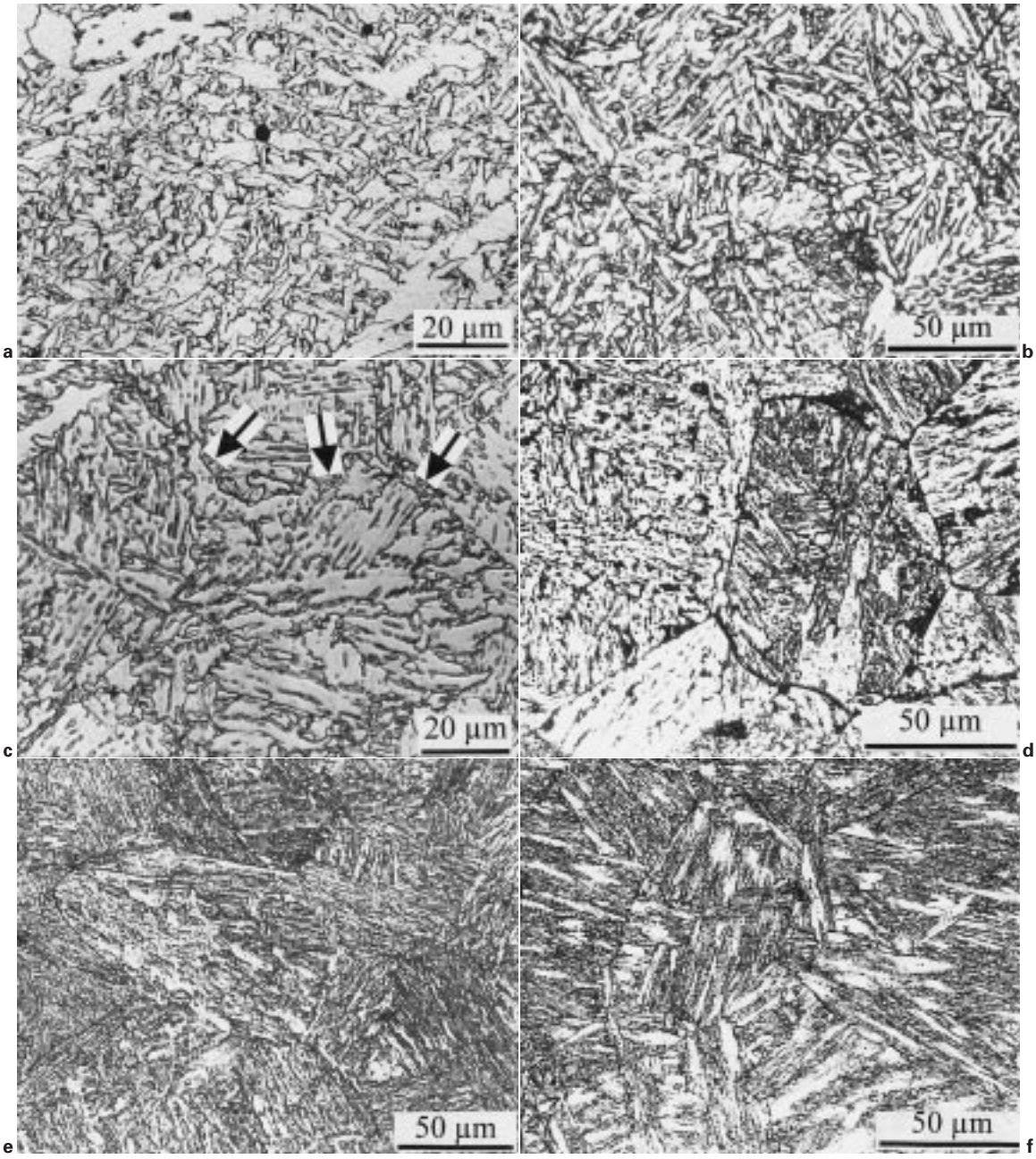

a acicular ferrite (specimens A1 and A2); *b* upper bainite, coarse grained heat affected zone (CGHAZ) (specimens B1 and B2); *c* upper bainite, intercritically reheated CGHAZ (specimens B3 and B4); *d* upper bainite (specimen C3); *e* lower bainite (specimen C2); *f* martensite (specimen C1)

1 Light micrographs of various steel microstructures after nital etching

inclusions (mostly titanium oxides) which are known to highly favour the nucleation of acicular ferrite with respect to bainite and Widmanstätten ferrite.[14,15] The average inclusion diameter was 0·4 μm. This material was provided as the top layer of a weld metal deposit. The thickness of the steel sheets used for welding was 30 mm. The metal was deposited by submerged arc welding with a welding energy of 2·01 kJ mm^{-1} and a cooling time between 700 and 300°C ($\Delta t^{7/3}$) of 80 s (*see* Table 2). The austenite grain size and the titanium content were high enough to ensure

Table 2 Heat treatments and resulting microstructures: PF polygonal ferrite; AF acicular ferrite; M–A martensite–austenite islands

Steel	Specimen	Heat treatment	Average austenite grain size, μm	Resulting microstructure
A	A1	As deposited weld metal $\Delta t^{7/3} \sim 80$ s	200*	PF + AF + pearlite
	A2	Same as A1 + 600°C for 4 h cooling 20°C h^{-1}	200*	PF + AF + carbides
B	B1, B2	Heating up to 1250°C (500°C s^{-1}) cooling $\Delta t^{7/3} = 100$ s	60	Bainite + carbides
	B3, B4	Same as B1 + heating 775°C (500°C s^{-1}), cooling $\Delta t^{7/3} = 100$ s	60	Bainite + M–A
C	C1	1100°C for 0·5 h, cooling at 4°C s^{-1}, tempering 630°C + step cooling	140	Martensite
	C2	Same as C1 but cooling at 1°C s^{-1}	140	Lower bainite
	C3	Same as C1 but cooling at 0·1°C s^{-1}	140	Upper bainite

*Columnar grains of average size 200 μm but up to 1 mm in length.

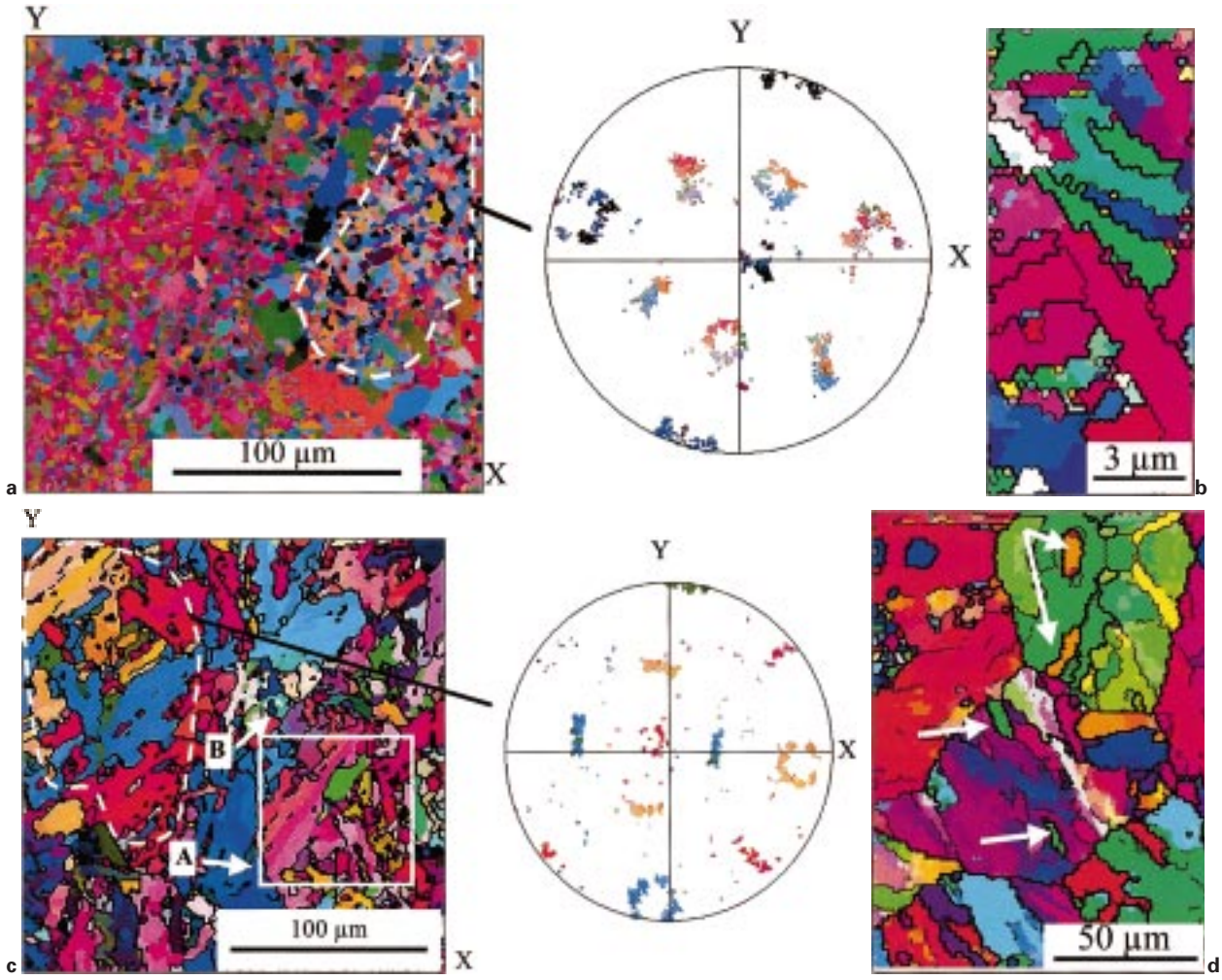

a acicular ferrite (specimen A2); *b* high resolution map of specimen A1, high angle boundaries ($>47^{\circ}$) between adjacent plates are highlighted; *c* upper bainite microstructure of steel B; *d* upper bainite microstructure of specimen C3, some small grains are embedded in larger ones and twin related to them (marked with arrows)

2 Electron backscattering diffraction maps and corresponding {002} pole figures of ferritic plates found within given former austenite grains

the formation of acicular ferrite along with the growth of some polygonal ferrite near the former austenite grain boundaries. Some specimens were also given a stress relieving heat treatment (4 h at 600°C).

Both specimens A1 and A2 exhibited nearly the same microstructure consisting of polygonal ferrite grown along the former austenite grain boundaries and interlocked, fine acicular ferrite platelets intragranularly nucleated on inclusions (Fig. 1*a*). The average and maximal aspect ratios of the acicular ferrite plates were measured in the plane of the polished section by image analysis. They were shown to be 1·75 and 4, respectively for both specimens A1 and A2. The presence of up to six different plate growth directions per austenitic grain suggested that the morphology of the acicular ferrite was not greatly influenced by stress.[16] However, as will be discussed later, the same conclusion could not be drawn concerning the crystallographic orientations of the ferritic plates.

The bainitic microstructure was studied in two conditions, i.e. as simulated heat affected zones (HAZs) of welds (steel B) and as quenched and tempered material (steel C). Steel B was used to simulate the bainitic microstructure encountered in the HAZs of high strength low alloy (HSLA) steels. Two heat treatments were applied to steel B using a Gleeble weld heat treatment simulator. The first heat treatment (specimens B1 and B2) was used to simulate the microstructure of the coarse grained HAZ (CGHAZ). The second heat treatment (specimens B3 and B4) was applied to simulate the intercritically reheated CGHAZ (ICCGHAZ) microstructure. Intercritical reheating at 775°C, i.e. between Ac_1 and Ac_3 led to a partial austenitisation of the bainitic microstructure. Further cooling led to the formation of the well-known martensite–austenite (M–A) constituent in these partially austenitised areas, which greatly decreases the toughness of the material.[17] Both microstructures consisted mainly of upper bainite as shown in Fig. 1*b* and *c*. The bainitic morphological packets were surrounded by carbides and nital etched boundaries for the simulated CGHAZ microstructure and also by M–A islands for the ICCGHAZ microstructure (marked with arrows in Fig. 1*c*). In order to assess the influence of the crystallographic properties on the cleavage fracture resistance, the specimens of steel B were longitudinally cut in fractured axisymmetrically notched specimens tested in the brittle fracture domain. The undeformed region was used to analyse the microstructure of the material. In addition, some secondary cracks, lying close to the fracture surface were also analysed by EBSD to assess the main microstructural feature controlling the cleavage crack propagation in this material.

Steel C was the same commercial A533 type steel as the material used by Raoul *et al.*[18] This steel was used to study martensite and bainite microstructures having the same chemical composition and prior austenite grain size. In

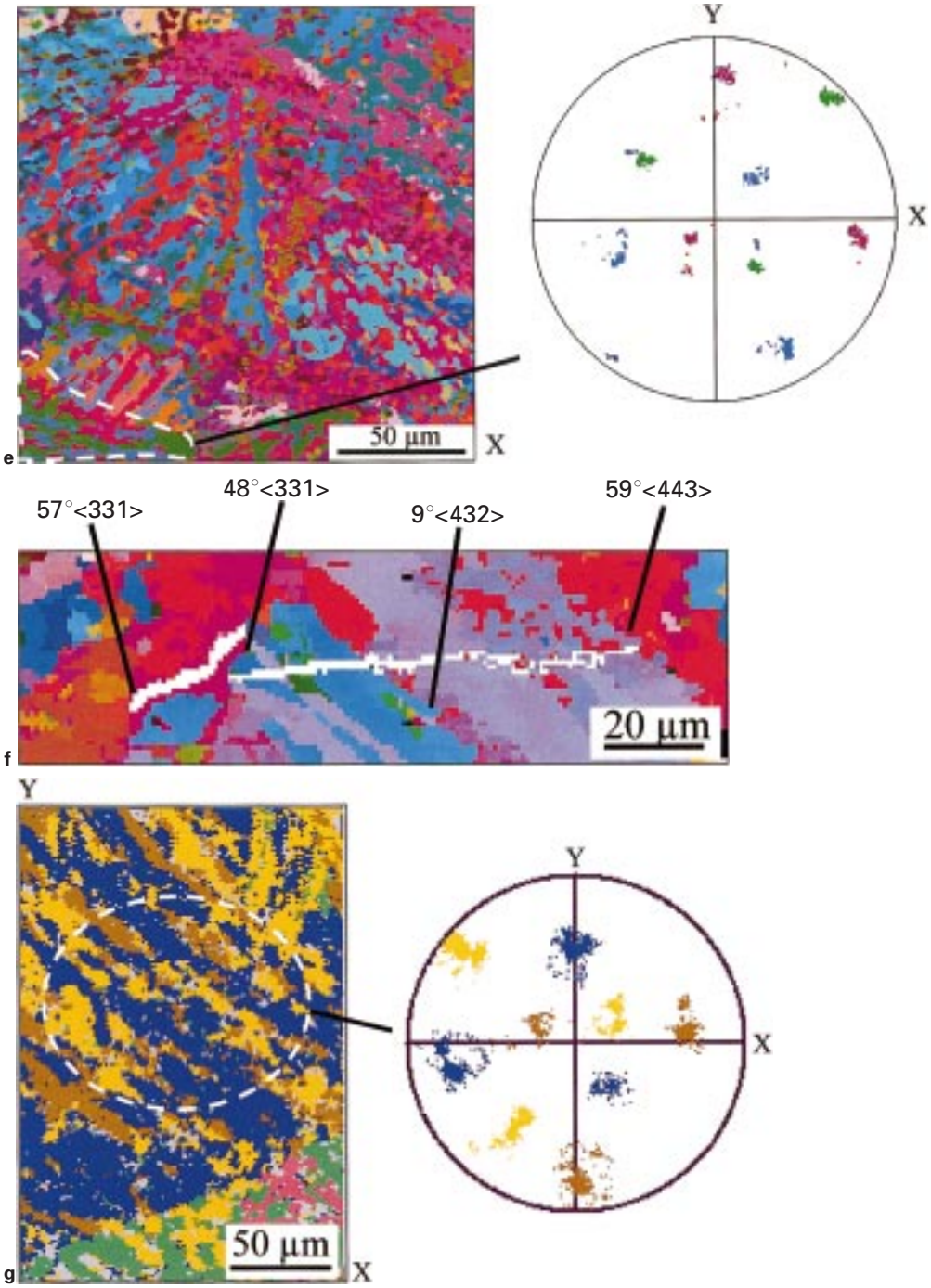

e lower bainite microstructure of specimen C2, most misorientation axis angle pairs correspond to twin relations; *f* secondary cracks in specimen B3 and axis angle pairs corresponding to boundaries encountered by cracks; *g* martensite microstructure of specimen C1

2 Electron backscattering diffraction maps and corresponding {002} pole figures of ferritic plates found within given former austenite grains (cont.)

addition, it is known to be sensitive to cleavage fracture and/or RTE. Its sensitivity to RTE strongly depends on the microstructure,[18] martensite and lower bainite microstructures being very sensitive whereas the upper bainite microstructure is insensitive. Thus, this material was studied with either bainitic (upper and lower bainite) or martensitic microstructures, as indicated in Table 2. For this purpose, three cooling conditions were chosen according to the continuous cooling transformation (CCT) diagram already published for this steel using the same austenitising conditions.[18] The heat treatment involving the last AFT was carried out in a dilatometer. The specimens were then subjected to the same RTE heat treatment as in Ref. 18. The microstructures of specimens C3 (upper bainite), C2 (lower bainite), and C1 (martensite) are shown in Fig. 1*d*, *e*, and *f*, respectively. All specimens were in fact longitudinally cut subsized Charpy specimens tested at -50°C in the brittle fracture domain as described by Raoul *et al.*[18]

EXPERIMENTAL PROCEDURE

All specimens were polished using diamond paste down to 0·25 μm grade. They were then electrochemically polished in a solution containing 70 vol.-% ethanol, 12 vol.-% distilled water, 10 vol.-% butanol, and 8 vol.-% perchloric acid, operating at 30 V and -30°C.

Most EBSD maps were obtained on a Jeol JSM 840–A SEM equipped with a conventional EBSD system. Some

specimens (A1, C1, and C3) were also analysed in a Zeiss DSM 982 SEM equipped with a field emission gun (FEG-SEM) giving a resolution better than 0·3 μm for local EBSD measurements and even better for secondary electron observation. Both SEMs were operated at 20 kV with the specimen tilted by 70°. After EBSD analysis, all specimens were etched in a 2 vol.-% nital solution and examined using light microscopy. Light micrographs were taken of all areas investigated with EBSD. Acicular ferrite specimens were also examined in the FEG-SEM for higher resolution EBSD measurements and secondary electron observation.

Results

Electron backscattering diffraction maps corresponding to the various microstructures studied are presented in Fig. 2, along with {002} pole figures of the ferritic crystallites within some former austenite grains. In this section, the results are discussed in relation to the microstructures studied.

In order to analyse the austenite to ferrite phase transformations, the crystallographic orientation relationships between the austenite and ferrite phases were investigated in the present study. Both the Kurdjumov–Sachs[19] (KS) and Nishiyama–Wassermann[20,21] (NW) crystallographic relationships were considered, although the AFT does not lead to exactly these relationships between austenite and ferrite. For both relationships, it is assumed that one $\langle 111 \rangle$ plane of the austenite phase is parallel to one $\langle 110 \rangle$ plane of the ferrite phase. The second part of the relationship is concerned with crystallographic directions in these parallel close packed planes, in the following way:

(i) for the KS relationship: one $\langle 111 \rangle_\alpha$ is parallel to one $\langle 110 \rangle_\gamma$
(ii) for the NW relationship: one $\langle 110 \rangle_\alpha$ is parallel to one $\langle 211 \rangle_\gamma$.

ACICULAR FERRITE

An example of EBSD results obtained with specimen A2 is presented in Fig. 2*a*. The plate boundaries were very difficult to analyse in the conventional SEM, owing to the overlapping of the Kikuchi patterns coming from the neighbouring ferrite grains. Thus, owing to the small size of the ferrite plates, the shape of the plates could not be accurately represented in the noise reduced image of Fig. 2*a*. This is easily seen if one compares the EBSD map of Fig. 2*a* with the light micrograph of the same area shown in Fig. 3*a*. However, in each former austenite grain three crystallographic orientations (or texture components) were observed for the ferrite plates. In the map of Fig. 2*a*, the colours correspond to the crystallographic orientation in the following way. The orientation of each analysed crystallite is given by the three Euler angles (ϕ_1, Φ, ϕ_2) in Bunge's representation. The angles ϕ_1, Φ, and ϕ_2 are represented by a value (ranging between 0 and 255) in the red, green, and blue colours, respectively. This allows the grain orientation to be represented in a convenient way. In the example of the right grain in Figs. 2*a* and 3*a*, three texture components can be seen in dark/blue (for texture component 1), grey/pink (for texture component 2) and also grey/pink (for texture component 3). The sketch in Fig. 3*c* shows that these texture components are highly misoriented. The three texture components were evenly distributed within all examined former austenite grains.

In spite of the small size of the plates, some of them were identified as having grown from the same inclusion, but with different crystallographic orientations. The high resolution SEM micrograph in Fig. 3*b* is typical of all inclusions found within the plane of the cross-section. It shows that the ferrite plates directly nucleated from the inclusions. In the high resolution (FEG-SEM) EBSD map in Fig. 2*b*, the grain boundaries corresponding to a misorientation angle (between neighbouring plates) greater than 45° have been highlighted. It is clear from Fig. 2*b* that ferritic plates may have the same morphological direction but very different crystallographic orientations. On the other hand, several ferrite plates, bearing different crystallographic orientations, may nucleate from the same inclusion. In fact, nearly all boundaries between acicular ferrite plates were found to be high angle boundaries with misorientation angles greater than 45°.

In addition to the numerous high angle plate boundaries, low angle boundaries were also found within the acicular ferrite plates. This could explain the scatter observed in the {002} pole figure in Fig. 2*a*. An example is shown in Fig. 4 in the same area as in Fig. 2*b*. In the map of Fig. 4*a*, only the boundaries are plotted. Bold lines represent the high angle boundaries (i.e. the boundaries having a misorientation angle greater than 45°) while thin lines represent low angle boundaries (with a misorientation angle less than 15°). In Fig. 4*b*, the misorientation angles between two neighbouring points (point-to-point) have been plotted along the line AB in Fig. 4*a*. The misorientation angle between point A and the current point along the line AB (point-to-origin) is also shown in Fig. 4*b*. One can see that most plate boundaries are high angle boundaries, with the exception of the 30° boundary, which is an artefact as will be explained later. A lot of small misorientation boundaries are observed within the ferritic plates. Such plots will be referred to as 'misorientation line plots'.

In summary, EBSD analysis showed that the acicular ferrite microstructure consisted of highly intricate, highly misoriented plates having internal low angle boundaries. Three texture components were found for ferrite in each former austenite grain.

BAINITE: MICROSTRUCTURAL PROPERTIES

Electron backscattering diffraction analysis of bainitic specimens B1 to B4 showed that each former austenite grain contains several bainitic crystallographic packets (Figs. 2*c* and 5*a*). The {002} pole figures were plotted for each individual former austenite grain. As for acicular ferrite, three texture components were identified in each former austenite grain, as illustrated in the {002} pole figure in Fig. 2*c*. This pole figure corresponds to the area delimited by the white dashed line in the EBSD map. In this case, the three texture components correspond to the blue/green, yellow, and red colours respectively. To illustrate the misorientation relationships between the ferrite grains, the results concerning another grain (area delimited by the white square in Fig. 2*c*) are schematically represented in Fig. 5*b*. Each texture component was represented by only one grey level in Fig. 5*b*, and by only one orientation in the {002} pole figure in the sample frame of Fig. 5*c*. In this example, the orientation of the former austenite grain was determined assuming near NW relationships between the austenite and ferrite phases (in fact, agreement with the KS relationships was less good for this example). The indices of the crystallographic axes were first determined according to the Euler angles of these texture components (Table 3). Then, the {022} pole figure was plotted for all texture components. As no common {022} pole was found it was deduced that the texture components did not arise from the same {111} plane of the austenite phase. The orientation of the former austenite grain was determined by an iterative method. Then, the misorientation relationships between austenite and ferrite were deduced from the $\{111\}_\gamma$, $\{022\}_\alpha$, and $\{211\}_\gamma$ pole figures. They were expressed as axis angle pairs using a low index approximation for the rotation axis. The angles between both theoretical and experimental

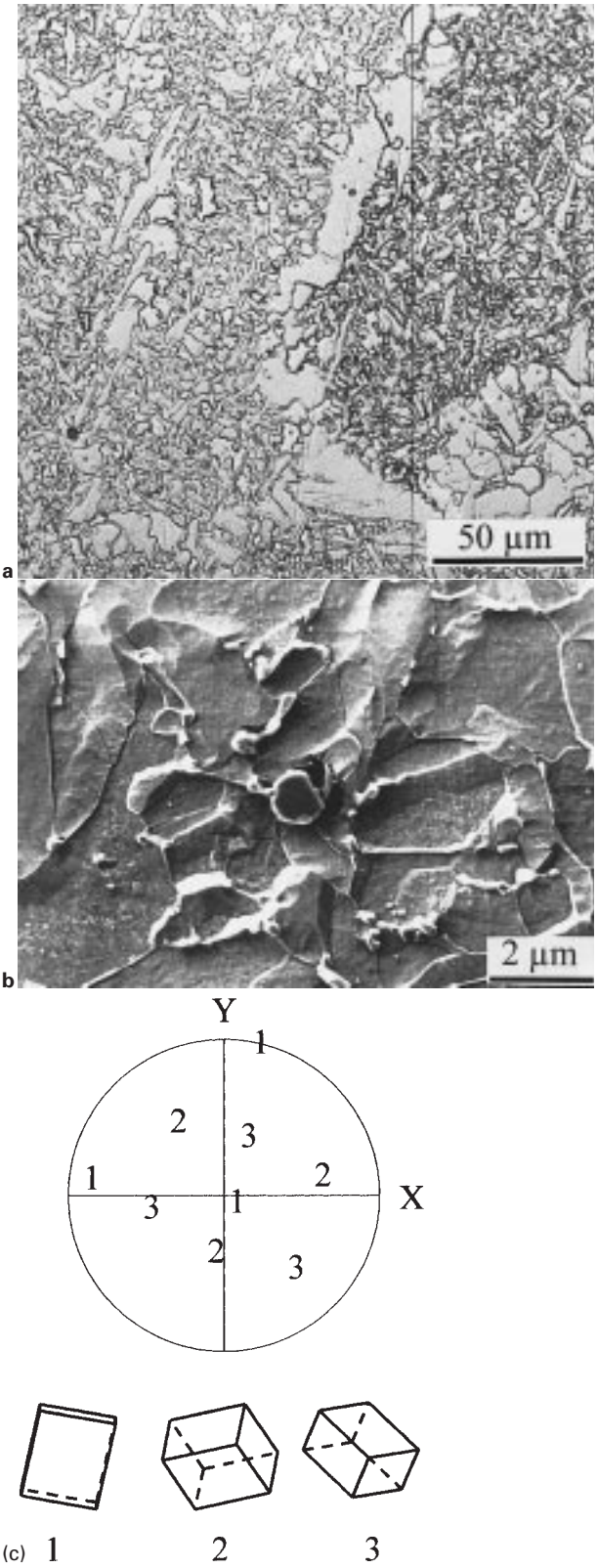

a nital etch micrograph of same area as in Fig. 2*a*; *b* high resolution SEM micrograph showing ferritic plates nucleated from same inclusion; *c* schematic {002} pole figure of texture components present in former austenite grain on right of *a* and corresponding orientations of ferrite crystals

3 Electron backscattering electron diffraction and SEM imaging results obtained with acicular ferrite microstructure

actual (i.e. not approximated) axes were then calculated. The results are shown in Table 3. The misorientation between the predicted and experimental ferrite crystal axes

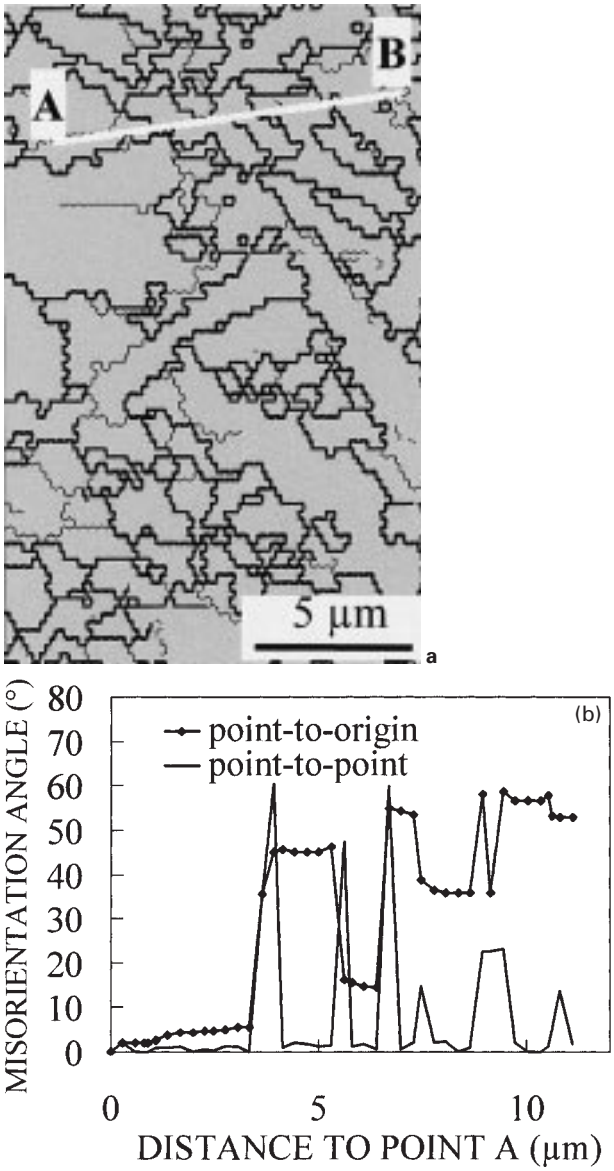

a high angle (>45°, bold lines) and low angle (<15°, thin lines) boundaries found in area in Fig. 2*b*; *b* corresponding misorientation line plot along line AB

4 Low angle boundaries observed within the acicular ferrite plates

does not exceed a few degrees, which is well within the scatter in the orientation measurements.

Most packet boundaries were high angle boundaries with misorientation angle values ranging between 47° and 60°. However, some small grains delimited by 30° and 45° boundaries were also found. Further analysis of the relevant Kikuchi pattern indexing procedure showed that these boundaries were an artefact owing to an error in the indexing of the pattern. This error occurred when the pattern mainly consisted of bands having a common intersection, in this case a ⟨111⟩ or a ⟨001⟩ zone axis. The problem arises from the fact that the indexing procedure requires another band that does not share the same intersection. For example, when a ⟨111⟩ zone axis is found in the middle of the pattern, and because of the particular features of the body centred cubic (bcc) structure of the ferrite crystal, one needs a very high quality pattern to find and correctly index such a band. If this is not the case, the software may wrongly index the bands sharing the common ⟨111⟩ zone axis, and owing to the geometric properties of the pattern, the resulting (wrong) orientation is always 30° ⟨111⟩ rotated from the right orientation. Such errors are

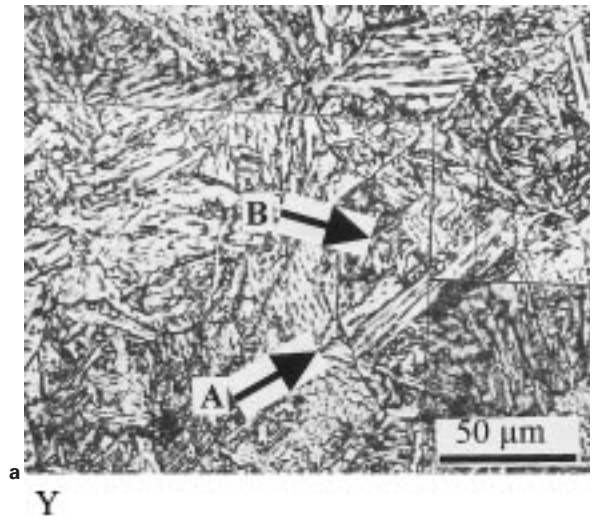

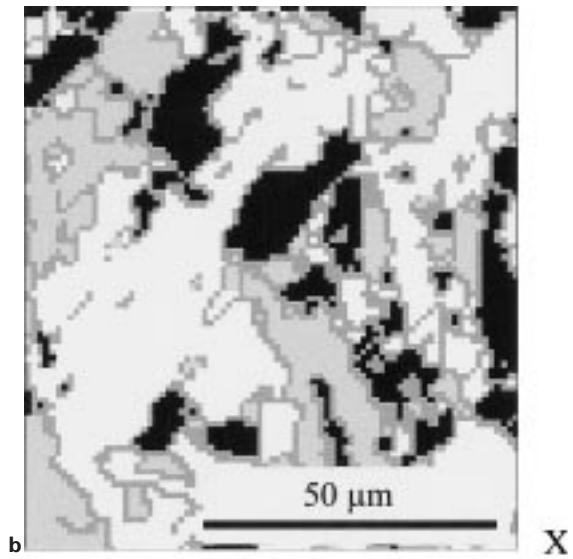

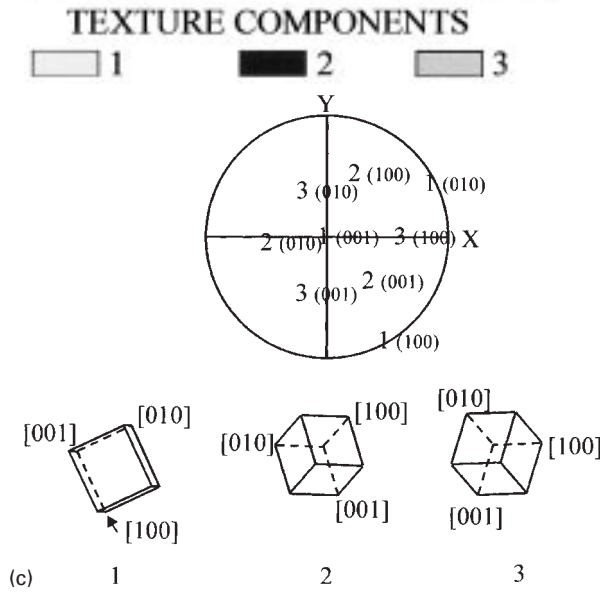

a nital etch micrograph, same area as in Fig. 2*c*; *b* detail of the texture components in one particular former austenite grain; *c* {002} pole figure for the texture components of the grain of *b* in the sample frame and corresponding orientation of the ferrite crystals

5 Analysis of EBSD results obtained with specimens of steel B: same area as in Fig. 2*c*

very difficult to avoid. In most cases, they result in small grains, which may be neglected in the analysis of the EBSD results. The only way to limit such errors is to further improve the quality of the Kikuchi patterns. In the present study, these 30° and 45° boundaries (which cannot be ferrite to ferrite boundaries within a given austenite grain, *see* below) were not considered in the analysis of the EBSD results.

Although the former austenite grain boundaries of specimens B3 and B4 were half covered with M–A islands up to a few micrometres in size, these islands were not detected in the EBSD maps as particular grains near the grain boundaries. This may be owing to (a) poor indexing of the areas very close to the grain boundaries, where two Kikuchi patterns overlap and (b) the small grain size and the very fine microstructure of these particles, which are often polycrystalline and/or heavily dislocated. This leads to further difficulties in indexing the EBSD patterns. Only high resolution EBSD could give crystallographic information about the relationship between the M–A constituent and the surrounding ferritic grains. Such investigations are currently in progress. Thus, only the bainitic component of the microstructure of steel B was considered in the present study.

For each area investigated, a comparison of the crystallographic and the morphological packets defined in the previous section was made. Figures 2*c* and 5*a* show that no one to one correspondence between both grain types could be found. The crystallographic packet may consist of several morphological packets (arrow A in Figs. 2*c* and 5*b*), and vice versa (arrow B in Figs. 2*c* and 5*a*). In particular, some apparently self-accommodating V shaped morphological packets were found to actually consist sometimes of one, and sometimes of several crystallographic packets. Thus, it was found that the crystallographic packets of steel B could not be studied by light microscopy, whereas such a study could be rather simple with EBSD mapping.

As was the case for the acicular ferrite microstructure, numerous low angle boundaries were found inside the crystallographic packets. Examples of this are shown in Fig. 6 for specimens B1 and B3, in the same way as in Fig. 4. The bainitic packets often consisted of 'subpackets' delimited by low angle boundaries. This could explain the scatter in the crystallographic orientations observed in the {002} pole figures (*see* Fig. 2*c*).

Electron backscattering diffraction analysis of specimen C3 also showed the existence of subpackets (Figs. 2*d* and 7*a*), except that in the plane of the polished section, some former austenite grains were covered with only one crystallographic packet, occasionally embedding some smaller ones (*see* arrows in Fig. 2*d*). In the latter case, the misorientation axis angle pair of the neighbouring packets was most frequently 60° ⟨111⟩ (i.e. twin relation) or 55° ⟨110⟩. As will be discussed below, this suggests that the bainitic packets formed with near Kurdjumov–Sachs relationships with the parent austenite phase and arose from the same $\{111\}_\gamma$ plane.[9] This was also the case for all morphological packets of specimen C2. Comparison of the EBSD map in Fig. 2*e* and the micrograph in Fig. 7*b* clearly shows that the crystallographic packet size is in some cases much bigger than the morphological packet size. In summary, the morphological packets were found to generally consist of one or several (morphological) sheaves of laths having the same crystallographic orientation. Adjacent packets had misorientation angles of 47–60° and were not often twin related, whereas small packets embedded in a larger one always formed from the same $\{111\}_\gamma$ as their neighbour, and were most frequently twin related to it. It is worth noting that the upper bainite microstructure of specimens B1–B4 and C3 mainly consisted of adjacent, highly misoriented (but not twin related) packets, whereas

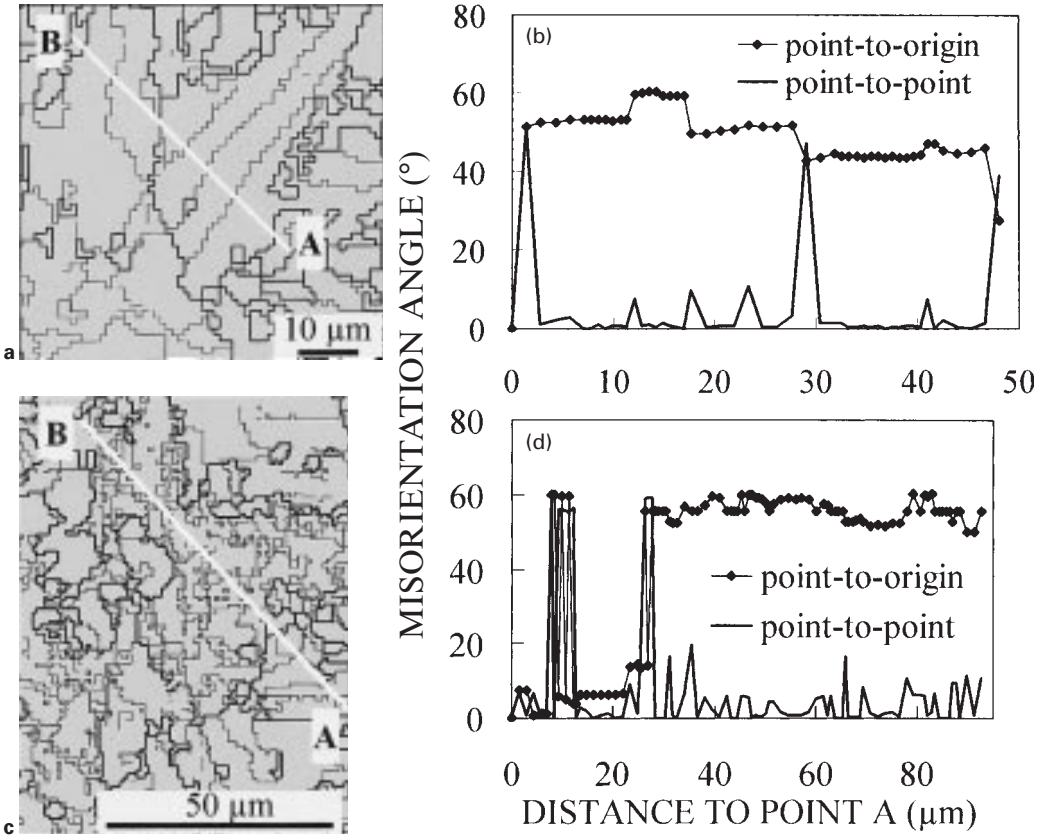

a specimen B1, high angle and low angle boundary map; *b* specimen B1, corresponding misorientation line plot; *c* specimen B3, high angle and low angle boundary map; *d* specimen B3, corresponding misorientation line plot

6 Low angle boundaries found in bainitic packets of steel B: same representation as in Fig. 4

the lower bainite microstructure of specimen C2 consisted of highly intricate, often twin related packets. This result will be further analysed in the 'Discussion' section below.

BAINITE: ANALYSIS OF CLEAVAGE CRACKS

Figures 2*f* and 8 show a typical example of a secondary crack analysed by EBSD. This specimen was tensile tested at −90°C until fracture. Crack deviation took place at all high angle boundaries corresponding to crystallographic packet boundaries. A total number of 65 packet boundaries were investigated in specimens of steel B tested between −170°C and −90°C. The influence of the misorientation between neighbouring crystallographic packets on secondary crack propagation is shown in Fig. 9. In the plane of the polished sections, crack deviation and/or arrest was observed at all boundaries having a misorientation angle greater than 45°. The case of the 43° misorientation angle was attributed to a former austenite grain boundary. On the other hand, a 10° misorientation never led to a noticeable deviation of the cleavage crack. Thus, the high angle packet boundaries were found to induce crack deviation. In conclusion, the crystallographic packet size, as presented in the following section, is a microstructural parameter of great significance with respect to cleavage cracking resistance of steel B. This is consistent with the results previously obtained by Bouyne *et al.*[9] with a 0·14C–2·25Cr–1Mo steel having a lower bainite microstructure.

MICROSTRUCTURE OF MARTENSITIC SPECIMEN

In each former austenite grain of specimen C1, the martensitic morphological packets were found to consist of highly intricate crystals showing three different crystallographic orientations and thus three texture components (Figs. 2*g* and 10*a*). In the example of Fig. 2*g*, the texture

Table 3 Example of Nishiyama–Wassermann relationships between austenite and upper bainitic ferrite in former austenite grain in Fig. 5

				Austenite to ferrite misorientation relationships			
	Euler angles, deg						
Texture component	ϕ_1	Φ	ϕ_2	Parallel close packed planes	Parallel directions	Experimental (low index) axis angle pairs	Angle between predicted and experimental (actual) axes, deg
1	267	5	45	$[1\bar{1}0]_\alpha$ $[\bar{1}\bar{1}1]_\gamma$	$[110]_\alpha$ $[2\bar{1}1]_\gamma$	42° $[1\bar{4}0]_\gamma$	1·7
2	41	51	42	$[01\bar{1}]_\alpha$ $[\bar{1}\bar{1}\bar{1}]_\gamma$	$[011]_\alpha$ $[\bar{1}12]_\gamma$	44° $[10\bar{4}]_\gamma$	4·7
3	331	52	41	$[0\bar{1}1]_\alpha$ $[\bar{1}\bar{1}1]_\gamma$	$[011]_\alpha$ $[\bar{1}21]_\gamma$	44° $[\bar{1}\bar{4}0]_\gamma$	2·1
γ grain	37	45	358	Theoretical axis angle pair between α and γ (NW): 46° ⟨410⟩			

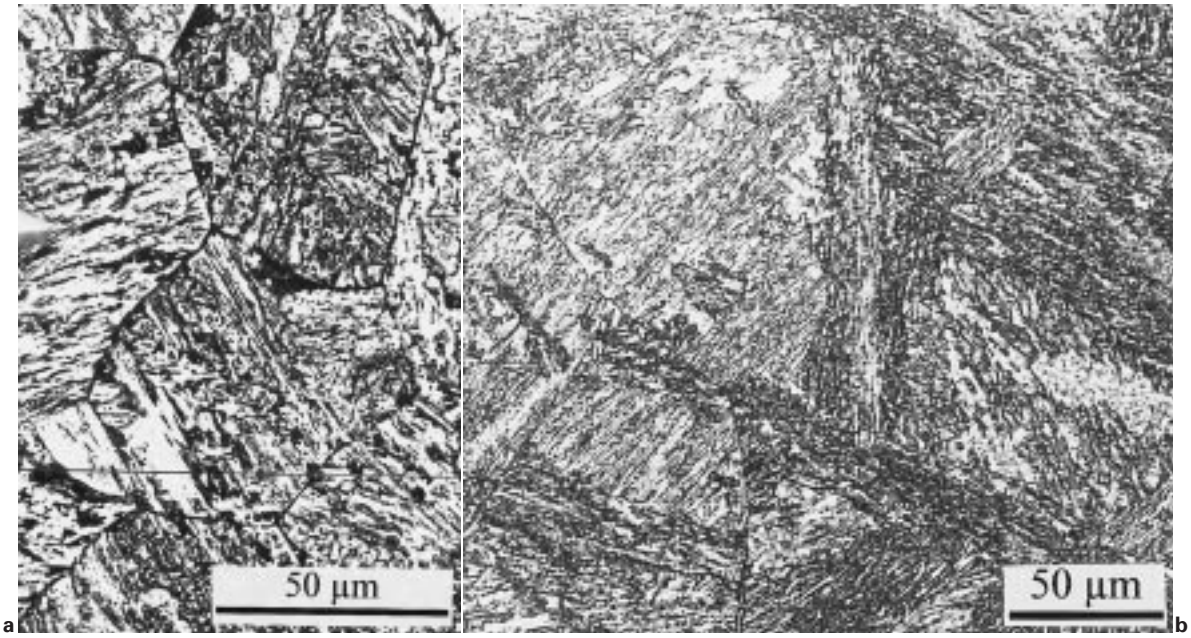

a specimen C3, same area as in Fig. 2*d*; *b* specimen C2, same area as in Fig. 2*e*

7 Light micrographs of bainitic specimens of steel C corresponding to EBSD maps of Fig. 2: nital etched

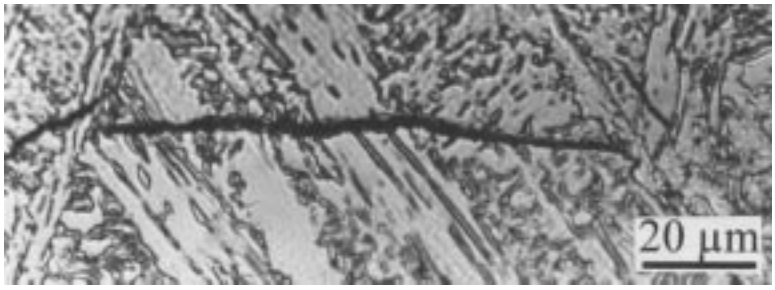

8 Nital etch micrograph of secondary cracks in specimen B3: corresponding EBSD map is shown in Fig 2*f*

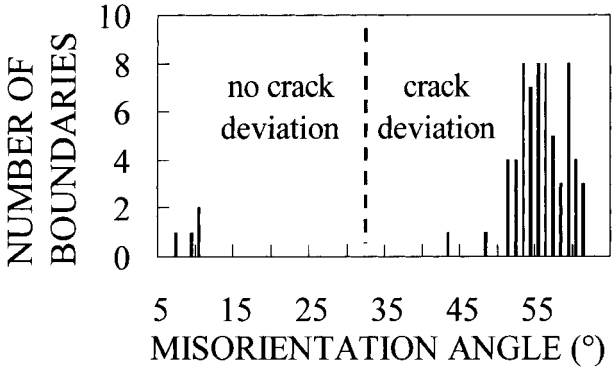

9 Histogram of misorientation angle distribution between neighbouring cracked grains in cracked areas: effect of misorientation angle on crack propagation and deviation

components were highlighted in the same (arbitrary) colours in both the map and the {002} pole figure. The corresponding orientations of the martensite crystals are schematically represented in Fig. 10*b*. As was the case for the other microstructures studied, a number of crystallographic packets were shown to contain low angle boundaries (Fig. 10*c* and *d*). This is consistent with the scatter in the orientations observed in the pole figures. For this microstructure, and in the plane of the cross-section, the morphological packet size was much bigger than the crystallographic packet size.

In this low carbon martensitic microstructure, the morphology of the crystallographic packets was found to correspond to the morphology of the 'blocks' defined by Maki *et al.*[22] using light microscopy. These authors distinguished between 'packets' (corresponding to the morphological packets defined in the present study) and 'blocks' (corresponding to the crystallographic packets defined in the present study, namely, in this case, groups of laths sharing the same morphological and crystallographic orientations). Each 'packet' was found to consist of one or several 'blocks'. This result does not confirm, however, the TEM observations published by Chilton *et al.*[23] and Sarikaya *et al.*,[24] who found that each individual lath could nucleate with one of the six crystallographic variants arising from the same $\{111\}_\gamma$, i.e. that the block size corresponded to the lath size. However, the high number of crystals analysed by EBSD in the present study provides good statistics which should be representative of the microstructure of steel C in the martensitic condition. As for specimens C2 and C3, the axis angle pair describing the misorientation between neighbouring grains of the same morphological packet was mainly 60° ⟨111⟩ and occasionally 55° ⟨110⟩. This suggests that within a given morphological packet, the crystallographic grains have a close packed plane parallel to the same $\{111\}_\gamma$ plane and are mostly twin related.

In view of the experimental results, it is interesting to assess how EBSD may provide useful quantitative information about the AFT mechanisms leading to the various microstructures studied and the fracture properties of these

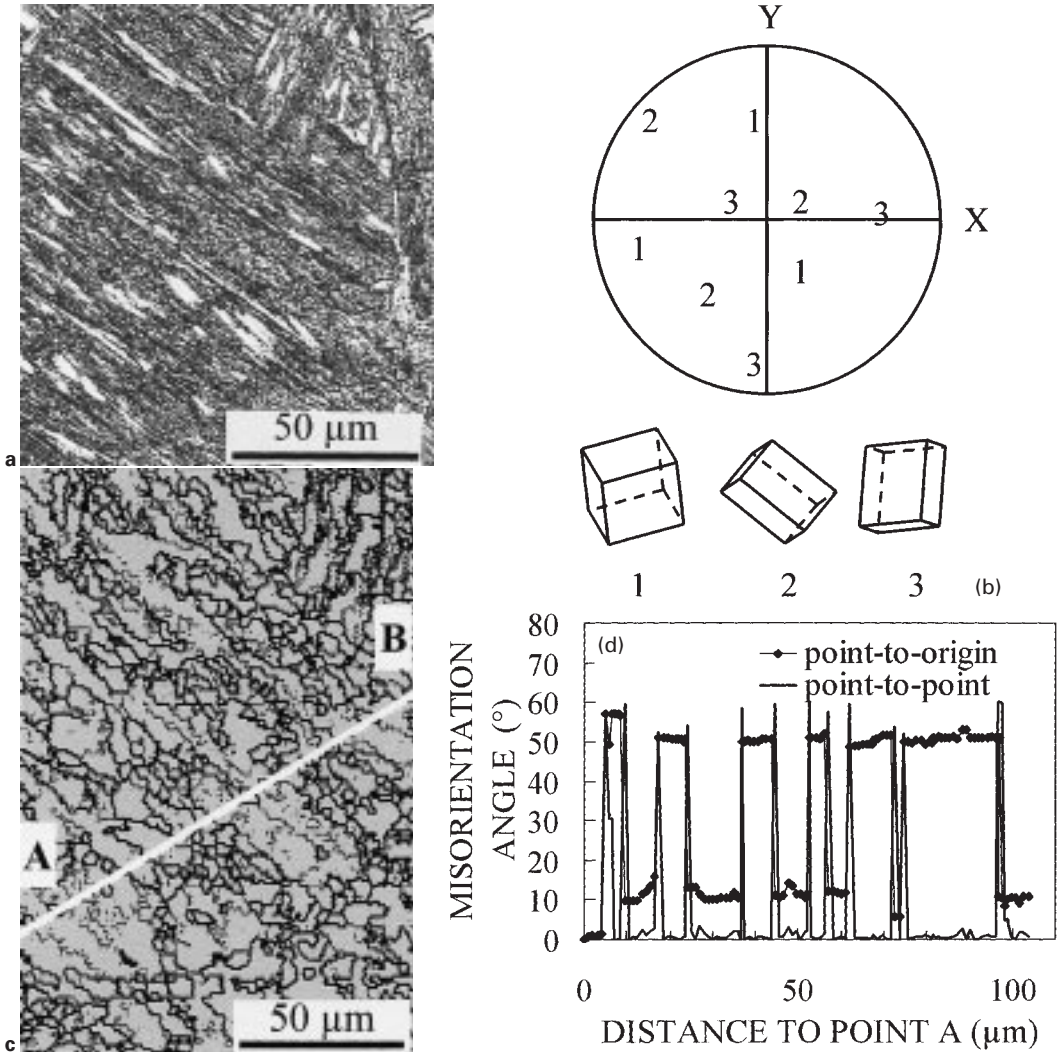

a nital etch micrograph, same area as in Fig. 2*g*; *b* schematic {002} pole figure and corresponding orientations of the martensitic crystals for grain on top of Fig. 2*g*; *c* high angle and low angle boundary map; same representation as in Fig. 4; *d* corresponding misorientation line plot

10 Analysis of EBSD results obtained with specimen C1

microstructures, in particular their resistance to cleavage and intergranular cracking. Both points will be addressed in the 'Discussion' section below.

Discussion

INFORMATION FROM EBSD ABOUT AUSTENITE TO FERRITE PHASE TRANSFORMATION

In order to analyse the information given by the EBSD maps more accurately, the misorientation relationships between adjacent grains nucleated in the same austenitic grains were expressed in terms of axis angle pairs. The theoretical axis angle pairs of neighbouring grains were also calculated for variants bearing either KS or NW crystallographic relationships with the same parent austenite phase. The misorientation angle distribution was then calculated, assuming that each variant had the same probability to form, i.e. assuming that there was no correlation between the crystallographic orientations of neighbouring variants. Details of the calculations are given in the Appendix.

The results are presented in Table 4 and Fig. 11. The actual rotation axes having irrational indexes were approximated by low index crystallographic axes. The misorientation angles (offset) between the actual axes and their corresponding low index axes are also given in Table 4. Figure 12 shows the experimental misorientation distribution histograms found with the various microstructures. Misorientation angles smaller than 5° were not represented in the experimental curves because they never corresponded to a packet boundary. They arose from the low angle boundaries found within the packets, as shown in Figs. 4, 6, and 10. In fact, for all studied microstructures, the internal structure of the packets is known to consist of a number of slightly misoriented groups of laths, in relation to the high dislocation density of these microstructures (*see* for example Bhadeshia[25] for the case of bainite).

It was checked on numerous grain boundaries, in particular on boundaries close to the secondary cracks of steel B, that the axis angle pairs actually corresponded to the ones reported in Table 4. This indicated that the KS and NW relationships, although never being exactly followed, were able to satisfactorily describe the misorientation angles between two ferritic grains in the steels studied. Thus, only KS and NW orientation relationships were considered in the present discussion.

The results of the present study confirm that there are strong similarities between microstructures formed at low temperatures, namely, lower bainite and martensite. There are also similarities between microstructures formed at higher temperatures, namely, acicular ferrite and upper bainite. The former will be referred to as LT microstructures, the latter as HT microstructures in the following discussion.

Table 4 Theoretical misorientation relationships between two ferrite grains formed from same austenite grain with Kurdjumov–Sachs (KS) or Nishiyama–Wassermann (NW) relationships: offset parameter is angle between actual rotation axis and low index approximated <*uvw*> axis

	Misorientation relationship																			
	Same $\{111\}_\gamma$				Two different $\{111\}_\gamma$															
KS/KS																				
Angle, deg	0	60	60	49·5	10·5	10·5	14·9	20·6	20·6	21·1	47·1	49·5	50·5	50·5	51·7	57·2	57·2			
Low index axis <*uvw*>	…	111	110	110	110	111	310	310	221	210	221	111	431	322	221	432	331			
Offset, deg	…	0	0	0	0	0	4·41	1·21	1·80	2·36	4·22	0	1·90	1·47	1·80	1·90	4·60			
Probability, %	4·17	4·17	8·33	4·17	4·17	4·17	8·33	4·17	4·17	4·17	8·33	4·17	8·33	8·33	4·17	8·33	8·33			
NW/NW																				
Angle, deg	0	60	…	…	13·8	19·5	50·0	53·7	…	…	…	…	…	…	…	…	…			
Low index axis <*uvw*>	…	110	…	…	110	100	443	331	…	…	…	…	…	…	…	…	…			
Offset, deg	…	0	…	…	3·45	0	0·13	0·76	…	…	…	…	…	…	…	…	…			
Probability, %	8·33	16·67	…	…	16·67	8·33	16·67	33·33	…	…	…	…	…	…	…	…	…			
KS/NW																				
Angle, deg	5·25	54·7	60·2	…	11·8	17·2	20·2	48·6	49·7	50·9	52·1	55·7	58·8	…	…	…	…			
Low index axis <*uvw*>	110	110	433	…	421	321	411	331	433	432	331	431	331	…	…	…	…			
Offset, deg	0	0	2·80	…	3·00	1·48	5·14	1·60	1·89	3·61	4·89	3·08	1·44	…	…	…	…			
Probability, %	8·33	8·33	8·33	…	8·33	8·33	8·33	8·33	8·33	8·33	8·33	8·33	8·33	…	…	…	…			

LOW TEMPERATURE MICROSTRUCTURES: MARTENSITE AND LOWER BAINITE

In the case of lower bainite and martensite microstructures, the misorientation relationships between the highly intricate crystallographic packets were found to be consistent with the packets bearing KS relationships with the parent austenite phase. The strong peak found for a misorientation angle $\theta = 60^\circ$ in Fig. 12*a*, together with analysis of the individual axis angle pairs corresponding to the packet boundaries show that most of the packets are in fact twin related, the axis angle pair describing the misorientation relationship (MR) being $60^\circ\ \langle 111\rangle_\alpha$. In the literature, the twin MR has been found to be associated with self-accommodating martensite variants, thus reducing considerably the shape strain induced by the martensitic transformation.[26,27] In addition, some authors (but not all) already found that the laths of a given morphological packet had KS orientation relationships with the parent austenite phase and all arose from the same $\{111\}_\gamma$.[26,27] Thus, the lower bainite and martensite formation mechanisms seem to share many common features, namely, the KS misorientation relationship between the parent and the product phase and highly intricate, twin related, self-accommodating crystallographic packets. This suggests that the AFT mechanisms could be very similar in both cases. Further studies are necessary, however, to confirm this hypothesis.

HIGH TEMPERATURE MICROSTRUCTURES: UPPER BAINITE AND ACICULAR FERRITE

The curves of Fig. 12*b* clearly showed that intercritical reheating of steel B did not influence the crystallographic properties (here, the misorientation between packets) of the bainitic microstructure. This was already expected, as only small areas of the material were transformed into austenite during reheating, leading to the formation of M–A islands which were not considered in the present study. Thus, no distinction will be made in the discussion between the various bainitic specimens of steel B.

The results of the present study suggest that, at least in terms of microtexture properties, upper bainite and acicular ferrite are in fact very similar, in agreement with observations made by previous authors.[28] In both cases, misorientation relationships between packets were found to be consistent with near NW orientation relationships between the parent and the product phase. This is illustrated in Fig. 12, where the peaks at 53–54° (labelled NW/NW) were interpreted using the data in Table 4. This misorientation angle and the corresponding axis angle pairs could best be accounted for assuming (near) NW/NW misorientation relationships. This suggests that packets grew with near NW relationships with the parent phase. In addition, the pole figures and the experimentally found axis angle pairs showed that within a given former austenite grain the packets did not necessarily arise from the same $\{111\}_\gamma$. This was also the case for adjacent packets in specimen C3, suggesting that these microtexture properties may be common to low carbon upper bainite and acicular ferrite microstructures of various chemical compositions.

Owing to the most frequently observed (near) NW/NW relationships between the crystallographic packets, twin relations were only found to occur rarely. In addition, most of the lath boundaries found within the bainite crystallographic packets were low angle boundaries, as already reported by Pickering.[29] The misorientation angle distributions were found not to correspond to the random distributions in Fig. 11, indicating that all variants did not have the same probability to form. In particular, some misorientation angles such as 20°, which were predicted to be highly probable (*see* Fig. 11) were never observed. In addition, three texture components were found in each

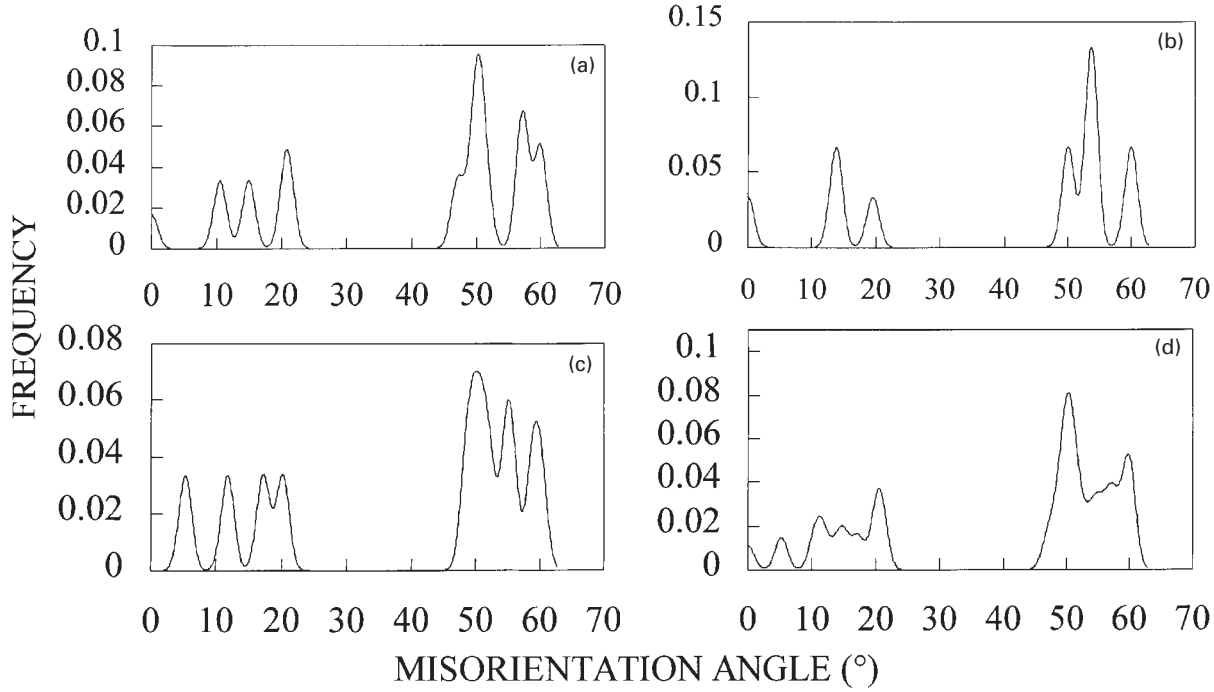

a KS and KS; *b* NW and NW; *c* KS and NW; *d* randomly KS or NW

11 Theoretical histograms of misorientation angle distributions calculated for two ferrite grains nucleated in same austenite grain with given relationships: all variants are assumed to have same probability to form

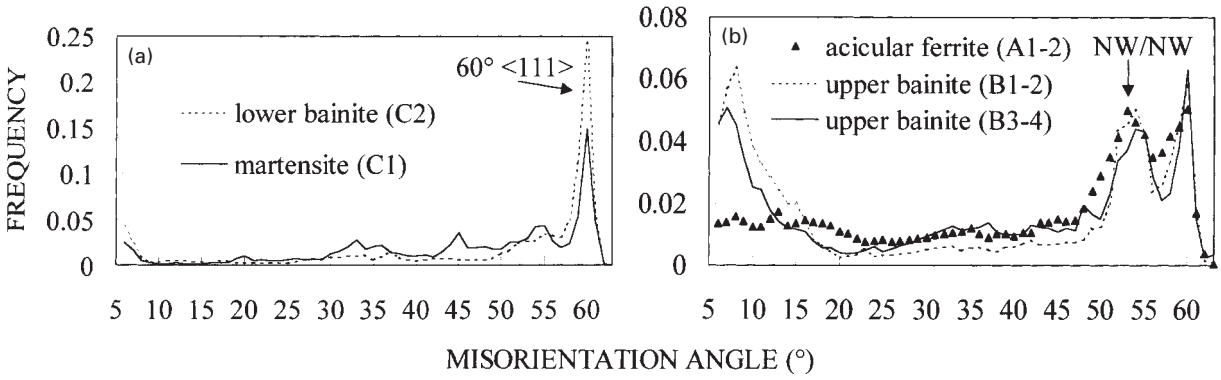

a martensite and lower bainite (steel C); *b* acicular ferrite (steel A) and upper bainite (steel B)

12 Histograms of experimental misorientation angle distributions obtained with steels A, B, and C

former austenite grain. This had been already observed with acicular ferrite[11] but not with bainite. This point will be discussed below, in relation to the local texture properties of lower bainite and martensite microstructures.

COMPARISON OF LT AND HT MICROSTRUCTURES

The main differences between LT and HT microstructures found in the present study are summarised in Table 5. In addition to the orientation relationships between the parent and the product phases, the morphology of the crystallographic packets and the microtexture properties have been reported. It is worth noting that upper and lower bainite microstructures differ not only in carbide distribution[29] but also in their crystallographic properties. This confirms the previous results obtained by Smith and Mehl[30] with eutectoid steels using X-ray pole figures. These authors showed that lower bainite and martensite had near KS relationships with the parent phase and that upper bainite had near NW relationships with the parent phase. The EBSD technique, however, allows such results to be

Table 5 Characteristics of steel microstructures investigated

Microstructure	Prominent α/α orientation relationships	α grains generally formed from same $\{111\}_\gamma$	Misorientation angles between α grains	Morphology of crystallographic packets	Microtexture in given former γ grain
Acicular ferrite	NW/NW	Not necessarily	47–60°	Plates	3 highly misoriented texture components
Upper bainite	NW/NW	Not necessarily	47–60°	Adjacent and intricate packets	
Lower bainite	KS/KS	Yes	50° and 60°	Highly intricate packets giving appearance of small grains	3 texture components (often twin related)
Martensite	KS/KS	Yes	50° and 60°		

obtained in a shorter time and on a finer scale than X-ray diffraction. Furthermore, it provides information about the grain distribution in space, at least on a two-dimensional basis and to study the microtexture of the material, i.e. its texture on a microstructural scale (here, within a given former austenite grain).

The microtexture properties may be represented by the pole figures obtained from the ferritic crystallographic packets in a given former austenite grain. Examples of such {002} pole figures are shown in Fig. 2 for the various microstructures investigated. They suggest that the microtexture properties of HT microstructures are very similar to those of the self-accommodating microtexture found in LT microstructures. Thus, it is worth noting that, although not necessarily coming from the same $\{111\}_\gamma$ and not being twin related, the upper bainite packets or acicular ferrite plates seem to form in a 'pseudo self-accommodating' manner. This is consistent with the fact that for both LT and HT microstructures investigated in the present study, the AFT mechanisms are claimed to be displacive, exhibiting a large shear component and a pronounced sensitivity of the crystallographic orientation to the local stress state.[25,31,32] It is thus possible that the non-random distribution may be owing to (a) an influence of the ferrite crystallographic orientation on the orientation of the neighbouring forming ferritic packets or (b) on a more global scale, to internal stresses appearing during the AFT. However, this is quite surprising as both upper bainite and acicular ferrite are supposed to nucleate from a number of separate sites (inclusions or grain boundaries) at the same time. In particular, the size of the acicular ferrite plates (up to a few tens of micrometres in length) is very small compared with the prior austenite grain size (up to a few millimetres in length). Thus, it cannot be assumed that the formation of the first acicular ferrite plates obviously influences the crystallographic orientation of the plates formed far away in the same austenite grain. Further studies, involving partially transformed microstructures, are needed to further address this point.

INFORMATION FROM EBSD ON MECHANICAL PROPERTIES OF STEEL MICROSTRUCTURES

As already pointed out by Katrakova *et al.*,[33] it is of great importance to correctly assess the crystallographic grain size, as this parameter greatly influences the strength and the cleavage fracture resistance of ferritic steels. The present study shows that EBSD is a very accurate and easy to use means of measuring the grain size, even for microstructures as fine as acicular ferrite or tempered martensite. In addition, it provides information about much larger areas than those investigated by TEM.

CLEAVAGE FRACTURE PROPERTIES

As most ferritic grains are highly misoriented, EBSD data can be used as input parameters in local approach fracture models to estimate the critical cleavage stress, along with the previously used information arising from either optical or transmission electron microscopy.[34,35] Such a model should be able to account for the high cleavage fracture resistance of tempered martensite and acicular ferrite compared with low carbon bainite.[36] In fact, as pointed out by Pickering,[29] the cleavage unit crack path corresponds to the distance between two neighbouring high angle boundaries, as these boundaries force the crack to deviate and to leave ligaments which are then fractured by ductile tearing. This leads to an increase in the crack propagation energy. More precisely, as most crystallographic packets found in both LT and HT microstructures are separated by high angle boundaries, the cleavage unit crack path was found to correspond to the crystallographic packet size in the present study. This explains the high resistance to cleavage fracture of the acicular ferrite, lower bainite, and martensite microstructures investigated in the present study compared with upper bainite. It confirms the results obtained by Yang *et al.*[36] with an ultra low carbon steel weld metal. Yang *et al.*[36] showed that even in the absence of carbides, the acicular ferrite microstructure was intrinsically tougher than the upper bainite microstructure and that the unit crack path was the ferritic plate or bainite packet size. The proposed mechanism implies, however, that no brittle phase forms at the ferrite grain boundaries, thus facilitating crack propagation across interfaces.

RESISTANCE TO INTERGRANULAR REVERSE TEMPER EMBRITTLEMENT

Many alloy steels suffer from reverse temper embrittlement (RTE) induced by impurity segregation at the grain boundaries, thus resulting in intergranular fracture. This phenomenon has been widely studied; a review of the main results has been recently published by Bulloch.[37] In particular, it affects low alloy A533 type steel plates such as those of steel C used in the present study. In fact, the bainitic and martensitic microstructures of steel C have been shown to exhibit large differences in their resistance to phosphorous induced RTE.[18] After the annealing and step cooling treatment, the fracture of martensitic Charpy specimens was always intergranular, whereas the fracture of bainitic Charpy specimens occurred by a cleavage mechanism.

By further examining the CCT diagrams presented by Raoul *et al.*,[18] it became clear that the transition in resistance to RTE coincides with the transition from upper bainite to lower bainite, and not from lower bainite to martensite microstructures. This result may tentatively be explained in the following way. The embrittling species (in this case phosphorus) are known to segregate at the high angle, highly disordered ferrite/ferrite interfaces like the former austenite grain boundaries. In addition, phosphorus may also segregate at the high angle packet boundaries found in the upper bainite microstructure. On the other hand, as the lower bainite and martensite packets are mostly twin related, the packet boundaries may be more ordered, in particular after local recovery occurring during the tempering heat treatment. However, this can only be a hypothesis, as the grain boundary structure, and in particular the orientation of the grain boundary plane, was not investigated in the present study. However, if it is actually the case, impurity segregation might not be favoured at these less disordered boundaries and impurities might only segregate at the former austenite grain boundaries. The local impurity level could then reach a critical value at the former austenite boundaries, leading to intergranular fracture as observed by Raoul *et al.*[18] This is not the case for upper bainite, as the numerous high angle packet boundaries provide efficient sinks for impurities, inducing a dilution effect, so that the critical impurity level may not be reached at any grain or packet boundary. Thus, although the numerous high angle boundaries between the twin related lower bainite and martensite packets promote resistance to cleavage crack propagation, they may induce a high sensitivity to RTE. This could explain why, in terms of sensitivity to RTE, and in the case of A533 steel plates tested at -50°C, the lower bainite microstructure exhibits a similar behaviour to martensite, but not to the upper bainite microstructure. This is owing to the crystallographic misorientation relationships between the packets and possibly to the structure of the packet boundaries.

Conclusions

Electron backscattering diffraction was proved to be a very powerful tool for examination of the microstructural

properties of fine steel microstructures in the present study, and led to the following conclusions.

1. The acicular ferrite microstructure under study consisted of fine plates directly nucleated on inclusions. Highly misoriented plates nucleated on the same inclusion, and plates having the same morphological direction could be highly misoriented. Almost all plate boundaries were high angle boundaries. In a similar way the upper bainitic microstructures consisted of adjacent, highly misoriented packets of laths.

2. Upper bainitic packets, or acicular ferrite plates, often formed from different $\{111\}_\gamma$ and exhibited misorientation angles lying between 47° and 60°. Their misorientation relationships were compatible with near Nishiyama–Wassermann misorientation relationships between austenite and ferrite. In particular, twin relations between adjacent packets were not often observed. In addition, numerous low angle boundaries were found within the crystallographic packets. There was no obvious correspondence between the crystallographic and the morphological packets but in many instances the crystallographic packets were found to contain several morphological packets. The cleavage unit crack path was found to be the distance between two consecutive high angle ferrite/ferrite boundaries, i.e. two crystallographic packet boundaries.

3. The martensitic and lower bainite microstructures consisted of highly intricate packets resulting in small crystallographic grains in the plane of the EBSD maps. The ferrite variants were frequently twin related and always formed from the same $\{111\}_\gamma$. Their misorientation relationships were consistent with near Kurdjumov–Sachs orientation relationships between austenite and ferrite.

4. For all microstructures, not all ferrite to ferrite misorientation relationships were represented, indicating that the ferritic packets or plates did not form randomly from a crystallographic point of view. In fact, in most former austenite grains three texture components were observed. Martensitic morphological packets generally have all three texture components, corresponding to small, highly misoriented twin related martensitic grains in the plane of the EBSD maps. This microtexture could be promoted as it favours the accommodation of shear stresses arising from the martensitic phase transformation. In the case of upper bainite and acicular ferrite, the microtexture was found to be very close to the self-accommodating microtexture of martensite. This could be owing to internal stresses, arising from the shear components of the austenite to ferrite transformation, influencing the crystallographic orientation of the newly nucleated ferrite variants. Further studies are necessary, however, to confirm this result.

5. In the case of the A533 type steel C, an attempt has been made to explain the difference in the sensitivity to reverse temper embrittlement of the 'lower temperature' (martensite and lower bainite) and 'higher temperature' (upper bainite) microstructures in terms of the difference in the misorientation relationships between neighbouring crystallographic packets. In the former case, embrittling impurities might only segregate at the former austenite grain boundaries, whereas in the latter case, the highly misoriented and disordered packet boundaries could provide efficient sinks for impurities, inducing a dilution effect and inhibition of intergranular embrittlement.

Appendix

Calculation of ferrite to ferrite misorientation relationships

In this Appendix, details are given about the calculation of the ferrite to ferrite misorientation relationships (MRs) presented in Table 4 and Fig. 11.

DETERMINATION OF FERRITE TO FERRITE MISORIENTATION RELATIONSHIPS

As explained in the text, two representative cases of the austenite to ferrite MRs have been chosen, namely, the Kurdjumov–Sachs[19] (KS) and the Nishiyama–Wassermann[20,21] (NW) MRs. The crystallographic relations between the parent and product phases are expressed as follows. In both cases one close packed plane of ferrite $\{110\}_\alpha$ is parallel to one close packed plane of austenite $\{111\}_\gamma$, for example $(011)_\alpha \| (111)_\gamma$. The second part of the relationship is concerned with directions contained in those parallel close packed planes:

(i) in the case of KS relationships: one $\langle 111\rangle_\alpha$ is parallel to one $\langle 110\rangle_\gamma$; in the present example, $[11\bar{1}]_\alpha \| [10\bar{1}]_\gamma$.

(ii) in the case of NW relationships: one $\langle 110\rangle_\alpha$ is parallel to one $\langle 211\rangle_\gamma$; in the present example, $[0\bar{1}1]_\alpha \| [\bar{1}\bar{1}2]_\gamma$.

As already pointed out by many authors, the closest variants having KS and NW relationships with the same parent grain only differ by a 5·25° rotation about the normal of the parallel close packed planes. There are 24 and 12 possible variants in the case of KS and NW relationships, respectively. The rotation matrices corresponding to all variants were calculated. Then, the rotation matrices describing the rotation between any ferritic variants were determined. Then, using the mathematical approach proposed by Lange[38] the MRs were expressed in terms of axis angle pairs for which the rotation angle was minimum. This procedure takes into account the cubic symmetry of the ferritic crystal. The corresponding rotation angles are reported in Table 4. To simplify the presentation, each rotation axis was also approximated with the closest low index axis having indices less than 5. The indices of the approximated axis and the 'offset' angle between both rotation axis and approximated low index axis are also reported in Table 4.

DETERMINATION OF MISORIENTATION ANGLE DISTRIBUTION BETWEEN TWO FERRITE VARIANTS

In order to calculate the misorientation angle distribution one must make assumptions concerning the probability for each variant to form. In the present study, it was supposed that all 24 variants of the KS type had the same probability to form, and that all 12 variants of the NW type had the same probability to form. Let P_{KS} (respectively P_{NW}) be the probability for a variant to be of the KS (respectively NW) type. If V_i is the ith variant of the KS type, and W_j is the jth variant of the NW type, one has the following equations for a ferritic grain of orientation G:

for i values of 1–24

$$P_{KS}(G = V_i) = P_{KS}/24$$

for j values of 1–12

$$P_{NW}(G = W_j) = P_{NW}/12$$

Four cases have been investigated, assuming the following orientation relationships between γ and α phases:

(i) both variants are of the KS type, i.e. $P_{KS} = 1$ and $P_{NW} = 0$ for both variants

(ii) both variants are of the NW type, i.e. $P_{KS} = 0$ and $P_{NW} = 1$ for both variants

(iii) one variant is of the KS type and the other of the NW type, i.e. $P_{KS} = 1$ (respectively 0) and $P_{NW} = 0$ (respectively 1) for the first variant (respectively for the second variant)

(iv) both variants are randomly of the KS or NW type, i.e. $P_{KS} = 24/(12 + 24) = 2/3$ and $P_{NW} = 12/(12 + 24) = 1/3$ for both variants.

For each case, for each ferrite to ferrite MR, the number of variants having that MR was calculated. Normalising the probability density of the variants gave the probabilities reported in Table 4. Then, the probability density was calculated considering only the misorientation angles, which may be common to several axis angle pairs (*see* Table 4). For example, an misorientation angle of 60° corresponds to two axis angle pairs, namely, 60° ⟨111⟩ and 60° ⟨110⟩. This gave the misorientation angle distribution function, which was a discrete sum of Dirac type peaks. Then, the distribution function was smoothed using Gaussian functions having a width of 1° corresponding to the accuracy of the EBSD measurements for misorientation angles. The curves plotted in Fig. 11 correspond to these 'theoretical' distribution functions for the misorientation angle between neighbouring grains.

Acknowledgements

Most of this work was carried out during a postdoctoral stay of one of the authors (AFG) at Imperial College (IC). This author thanks IC for providing her with EBSD facilities. She also thanks F. Grillon from Ecole Nationale Supérieure des Mines de Paris (ENSMP) for allowing her to use the FEG-SEM EBSD facility. Thanks are also due to D. Kaplan, T. Sturel, T. Iung, P. Maugis (IRSID), and to S. Raoul and B. Marini at the Commissariat à l'Energie Atomique (CEA) who proposed the use of and supplied steels A, B, and C for the study. Special thanks are due to Professor A. Pineau and to A. Lambert (ENSMP) for many fruitful discussions and to Dr E. Bouyne (ENSMP) for help with the crystallographic calculations.

References

1. V. RANDLE: 'Microtexture determination and its applications'; 1982, London, The Institute of Materials.
2. D. J. DINGLEY and V. RANDLE: *J. Mater. Sci.*, 1992, **27**, 4545–4566.
3. V. RANDLE: *Ironmaking Steelmaking*, 1994, **21**, (3), 209–214.
4. L. LAHN and K. KOPAL: *Prakt. Metallogr.*, 1996, **33**, (10), 516–530.
5. C. LINEAU, C. REY, and P. VIARIS DE LESEGNO: *Mater. Sci. Eng. A*, 1997, **A234–236**, 853–856.
6. A. J. WILKINSON and D. J. DINGLEY: *Acta Metall. Mater.*, 1991, **39**, (12), 3047–3055.
7. T. BAUDIN, Y. CHASTEL, and R. PENELLE: *Rev. Métall., Cah. Inf. Tech.*, May 1998, **95**, 611–620.
8. C. O. A. SEMPRIMOSCHNIG, J. STAMPFL, R. PIPPAN, and O. KOLEDNIK: *Fatigue Fract. Eng. Mater. Struct.*, 1997, **20**, (11), 1541–1550.
9. E. BOUYNE, H. M. FLOWER, T. C. LINDLEY, and A. PINEAU: *Scr. Mater.*, 1998, **39**, (3), 295–300.
10. M. G. HALL and H. I. AARONSON: *Metall. Mater. Trans. A*, 1994, **25A**, 1923–1931.
11. A. O. KLUKEN, Ø. GRONG, and J. HJELEN: *Metall. Trans. A*, 1991, **22A**, 657–663.
12. E. KANTIDIS: 'Rupture fragile intergranulaire d'un acier faiblement allié, approches globale et locale', PhD thesis, Ecole des Mines de Paris, 1993.
13. D. TIGGES: 'Nocivité des défauts sous revêtement des cuves de réacteurs à eau sous pression', PhD thesis, Ecole des Mines de Paris, 1995.
14. G. THEWLIS: *Mater. Sci. Technol.*, 1994, **10**, 110–125.
15. J. M. GREGG and H. K. D. H. BHADESHIA: *Acta Mater.*, 1997, **45**, (2), 739–748.
16. S. S. BABU and H. K. D. H. BHADESHIA: *Mater. Sci. Eng. A*, 1992, **A156**, 1–9.
17. B. C. KIM, S. LEE, N. J. KIM, and D. Y. LEE: *Metall. Trans. A*, 1991, **22A**, 139–149.
18. S. RAOUL, B. MARINI, and A. PINEAU: *J. Nucl. Mater.*, 1998, **257**, 199–205.
19. G. KURDJUMOV and G. SACHS: *Z. Phys.*, 1930, **64**, 325–343.
20. Z. NISHIYAMA: *Sci. Rep. Res. Inst. Tôhoku University*, 1934, **23,** 637.
21. G. WASSERMANN: *Arch. Eisenhüttenwes.*, 1933, **6**, 347–351.
22. T. MAKI, K. TSUZAKI, and I. TAMURA: *Trans. Iron Steel Inst. Jpn*, 1980, **20**, 207–214.
23. J. M. CHILTON, C. J. BARTON, and G. R. SPEICH: *J. Iron Steel Inst.*, 1970, **208**, 184–193.
24. M. SARIKAYA, H. TOKUSHIGE, and G. THOMAS: Proc. Conf. 'ICOMAT', Tokyo, 1986, The Japan Institute of Metals, 613–618.
25. H. K. D. H. BHADESHIA: 'Bainite in steels'; 1992, London, The Institute of Materials.
26. P. M. KELLY: *Acta Metall.*, 1965, **13**, 635–646.
27. P. M. KELLY: *Mater. Trans., JIM*, 1992, **33**, 235–242.
28. J. R. YANG and H. K. D. H. BHADESHIA: *J. Mater. Sci.*, 1991, **26**, 839–845.
29. F. B. PICKERING: Proc. Symp. 'Transformation and hardenability in steels'. Ann Harbor, MI, February 1967, Climax Molybdenum Co. and The University of Michigan, 109–129.
30. G. V. SMITH and R. F. MEHL: *Trans. AIME*, 1942, **150**, 211–226.
31. G. J. REES and P. H. SHIPWAY: *Mater. Sci. Eng. A*, 1997, **A223**, 168–178.
32. J. R. YANG, C. Y. HUANG, C. F. HUANG, and J. H. AOH: *J. Mater. Sci.*, 1995, **30**, 5036–5041.
33. D. KATRAKOVA, C. MAAS, D. HOHNERLEIN, and F. MUCKLICH: *Prakt. Metallogr.*, 1998, **35**, (1), 4–20.
34. J. P. NAYLOR and P. R. KRAHE: *Metall. Trans.*, 1974, **5**, 1699–1701.
35. P. BROZZO, G. BUZZICHELLI, A. MASCANZONI, and M. MIRABILE: *Met. Sci.*, 1977, 123–129.
36. J. R. YANG, C. Y. HUANG, C. F. HUANG, and J. H. AOH: *J. Mater. Sci. Lett.*, 1993, **12**, 1290–1293.
37. J. H. BULLOCH: *Mater. High Temp.*, 1994, **12**, 311–321.
38. F. F. LANGE: *Acta Metall.*, 1967, **15**, 311–318.